Moment tensor inversion of microearthquakes along the Santorini-Amorgos zone: Tensile faulting and emerging volcanism in an extensional setting

R. Andinisari [a,*], K.I. Konstantinou [a], P. Ranjan [a,b]

[a] *Department of Earth Sciences, National Central University, Chungli, Taoyuan, Taiwan*
[b] *Taiwan International Graduate Program–Earth System Science (TIGP–ESS), Taipei, Taiwan*

ARTICLE INFO

ABSTRACT

The Santorini-Amorgos zone is an area rich in microseismicity at the center of the Hellenic volcanic arc. The microseismicity of the zone is distributed along the Santorini-Amorgos ridge and Kolumbo submarine volcano. In this study, we utilized crustal events that were recorded by temporary networks during September 2002 to July 2004 and October 2005 to March 2007, and also by the permanent network from 2011 to 2020. These events were inverted for their moment tensors by using P-wave polarities as well as SV/P and SH/P amplitude ratios, yielding 74 well-constrained moment tensor solutions. Most of these moment tensors have significant CLVD and isotropic components that are positively correlated to each other ($R^2 = 0.68$). Tensile faulting due to high pore pressure is considered as the most likely cause of the observed non-DC components. The positive and negative non-DC components observed in Kolumbo may be generated by the opening and closing of cracks beneath the shallow (6–7 km) magma chamber due to a steady migration of magmatic fluids from the deep reservoir into the chamber. In Anydros, most of the microearthquakes have positive non-DC components associated with the opening of cracks. It is possible that the extensional deformation and high pore fluid pressure in the area opens subvertical cracks that become pathways for upward migrating fluids. The upward migration of magmatic fluids in an extensional regime such as the Santorini-Amorgos zone can also be viewed as an indication of emerging volcanic activity in this area.

© 2021 Elsevier B.V. All rights reserved.

1. Introduction

The complex geologic setting of the Aegean is characterized by two dominant tectonic processes. The first is the northward movement and subduction of the African plate beneath the Aegean at a rate of 0.9 cm/year (Reilinger et al., 2010; McClusky et al., 2000), resulting in the formation of the Hellenic subduction zone. The second is the southward migration of the Aegean plate due to the African slab rollback. This movement, coupled with the westward extrusion of the Anatolian plate, has resulted in the southwestward motion of the Aegean at a rate of 3.5 cm/year (Le Pichon et al., 1995; McClusky et al., 2000; Nyst and Thatcher, 2004; Hollenstein et al., 2008; Reilinger et al., 2010; Rontogianni, 2010) as seen in Fig. 1. The subduction of the African plate formed the Wadati-Benioff zone in the southern Aegean which extends down to about 170 km (Papazachos et al., 2000). The southern Aegean itself is a region where high seismicity is occurring along the

forearc. On the other hand, the back-arc region is characterized by moderate seismicity except from its eastern part (Dimitriadis et al., 2010). The boundary between the seismically active eastern and less active western back-arc region is the SW-NE oriented Santorini-Amorgos zone, where in 1956 two strong earthquakes occurred. One of these events had a seismic moment of 3.9×10^{20} Nm as computed by Okal et al. (2009) and was one of the largest earthquakes to strike Greece in the 20th century. Aside from the 1956 earthquakes, the Santorini-Amorgos zone has also experienced moderate to large earthquakes in the last 100 years with moment magnitudes ranging from 5.4 to 6.1 (see Andinisari et al., 2021).

The subduction of the African plate beneath the Aegean is also responsible for the formation of volcanic centers, one of which is Santorini caldera. Santorini is one of the most active volcanic centers in the southern Aegean and its largest eruption occurred around the year 1613 BCE. The eruption was followed by several smaller eruptions, resulting in the present-day Santorini caldera and the small islands in its center, namely Nea and Palea Kameni (Friedrich, 2013; Nomikou et al., 2014). The most recent activity of Santorini caldera was observed at the beginning of 2011 in the form of intense microseismic events that originated beneath
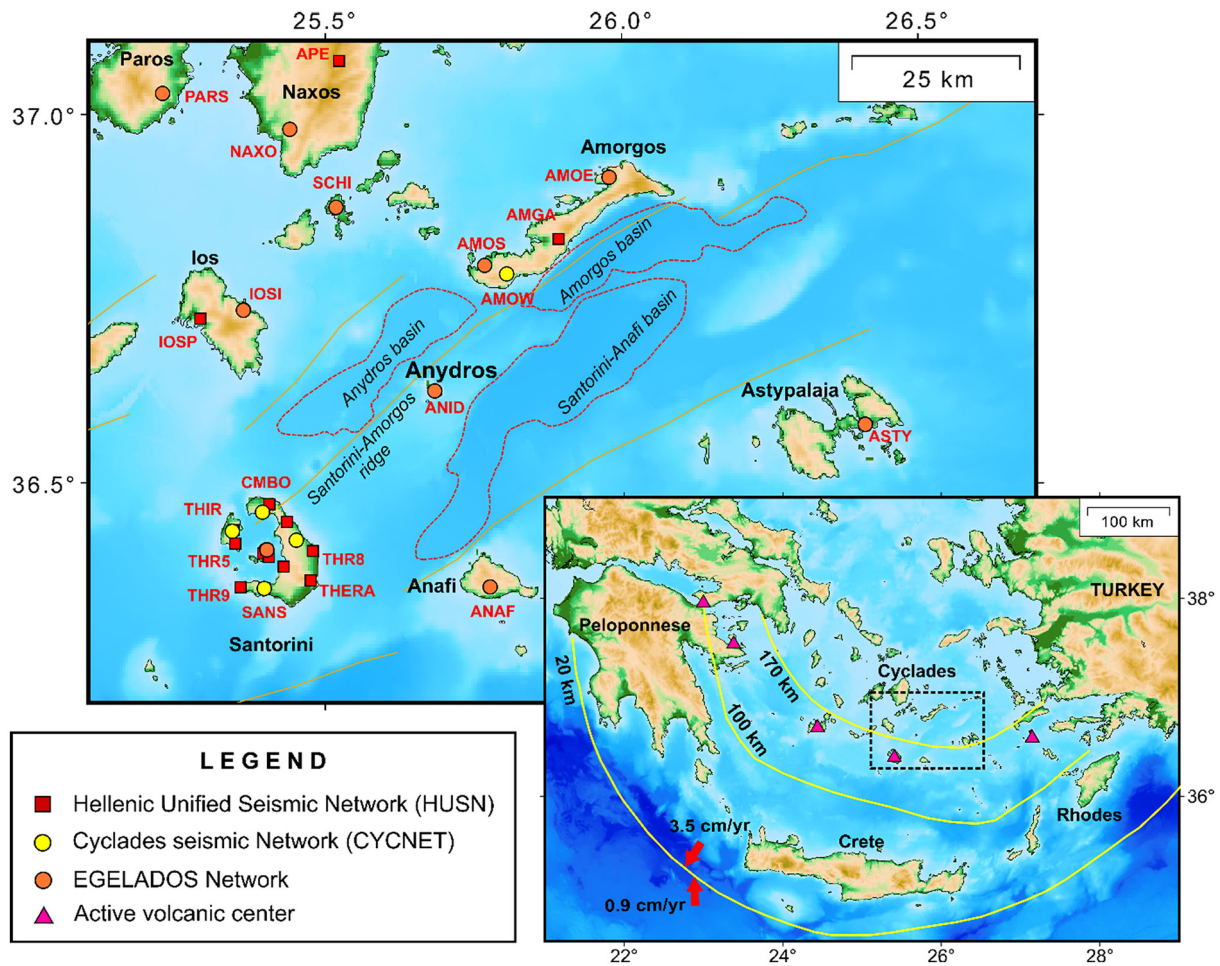
Fig. 1. Map of the South Aegean where the study area is shown by the dashed black square and enlarged in the top panel. Solid orange lines are fault traces contained in the GreDaSS database (Caputo and Pavlides, 2013). Dashed red lines indicate the boundaries of the basins in the area taken from swath bathymetry data (Nomikou et al., 2014). Solid yellow lines represent isodepth curves of earthquake hypocenters along the Southern Aegean Wadati-Benioff zone (Papazachos et al., 2000). The present-day plate motions are indicated by the red arrows (Reilinger et al., 2010). (For interpretation of the references to colour in this figure legend, the reader is referred to the web version of this article.)

the caldera, which ceased in the spring of 2012 (Konstantinou et al., 2013 and references therein). The Santorini-Amorgos zone also hosts Kolumbo submarine volcano located about 7 km NE of Santorini. The volcanic crater of Kolumbo has an oval shape with a diameter of 1700 m and a crater depth of 505 m (Nomikou et al., 2012; Hübscher et al., 2015). The most recent eruption of Kolumbo occurred in 1650 CE involving a pyroclastic flow and generating a tsunami that reached the east coast of Thera, which is the largest island in the Santorini complex (Cantner et al., 2014). Previous studies found significant microseismic activity beneath Kolumbo down to a depth of 19 km, with the bulk of the seismicity located at depths of 8–16 km. Considering that the magma chamber beneath Kolumbo probably lies at 6–7 km depth, the observed microseismicity was most likely related to the movement of melt from a deep reservoir to the shallow magma chamber (Bohnhoff et al., 2006; Dimitriadis et al., 2010; Konstantinou, 2020; Andinisari et al., 2021). Aside from this, swath bathymetry data revealed that there are 25 other smaller volcanic craters distributed along NE and NNE trends with respect to Kolumbo (Hooft et al., 2017). Pure CO_2 degassing along with small concentrations of CH_4 and H_2 were observed at Kolumbo and these smaller volcanic craters (Carey et al., 2015). Despite located very close to each other, geochemical studies have revealed that Kolumbo and Santorini have different magmatic sources (Klaver et al., 2016).

Crustal seismicity of the Santorini-Amorgos zone is concentrated along the Santorini-Amorgos ridge and beneath Kolumbo submarine

volcano (Bohnhoff et al., 2006; Andinisari et al., 2021). The observed seismicity has no clear relationship with the major faults in the area and is possibly triggered by fluid movement that generates earthquakes with smaller magnitude (Andinisari et al., 2021). Moment tensor inversion could help to clarify whether the seismicity is caused by pure shear faulting (double couple or DC source) or by other sources (non-DC) related to fluid intrusion. A common method is to decouple the source and the propagation effects by determining the response of the medium between the hypocenter and the seismic stations by calculating the Green's function. Then, the moment tensor solution is estimated by finding the minimum misfit between the actual and the synthetic seismograms. This approach was used to invert the moment tensors of two earthquakes that occurred near Kolumbo on 26 June 2009 (Mw of 4.9 and 4.7) with hypocentral depths of 9.7 km and 4.1 km. The resulting moment tensor solutions showed that both earthquakes had a significant isotropic component (Křížová et al., 2013). However, the use of Green's functions is limited for events at low frequency (~0.1 Hz) and will not be accurate for higher frequencies due to the complicated 3D structure of the medium (Julian et al., 1998). Therefore, this method is not suitable for microseismic events with Mw < 3 since these events lack energy in lower frequencies. The use of P-wave polarities and amplitude ratios of SV/P, SH/P, or SV/SH to determine the source mechanism is considered as one solution to this problem. This method also eliminates the instrument response owing to the use of amplitude ratios rather than absolute

amplitudes (Julian et al., 1998; Foulger et al., 2004; Jechumtálová and Šílený, 2005; Guilhem et al., 2014).

In a previous work, Andinisari et al. (2021) investigated the role played by fluids in the Santorini-Amorgos zone by using raypath Vp/Vs ratios and by calculating various petrophysical parameters (Poisson's ratio, crack density, fluid saturation). In this study, we investigate further the presence of fluids and their role in shaping the microseismicity in the area by utilizing the inversion of polarities and amplitude ratios for the determination of full moment tensor solutions of microearthquakes. We selected well-constrained events from the absolute locations of Andinisari et al. (2021) and supplemented them with the absolute locations of events that occurred throughout 2020. Then, moment tensor inversion was performed by utilizing P-wave polarities, and SV/P, SH/P amplitude ratios. We also plotted the derived moment tensors along with precise relative locations of microearthquakes published by Andinisari et al. (2021) and investigate the relationship between the moment tensors and the seismicity distribution. The results of moment tensor decomposition show that most of the inverted events have significant non-DC components that are likely related to fluid intrusion as also indicated by vertical earthquake clusters beneath the island of Anydros and the NE segment of the Santorini-Amorgos fault.

2. Data and earthquake locations

The crustal seismicity that occurred along the Santorini-Amorgos zone was recorded by three different seismic networks. The first is the Cyclades seismic Network or CYCNET that was deployed on the Cyclades island group from September 2002 to July 2004. This temporary network consisted of 16 stations with three-component short-period sensors (1-Hz MARK 4 L-3C) and 6 stations with broadband three-component seismometers (STS-2) (Bohnhoff et al., 2004). Second, EGELADOS (Exploring the GEodynamics of subducted Lithosphere using an Amphibian Deployment Of Seismographs) that consisted of 56 stations equipped with three-components sensors (45 Güralp 50-s, 4 STS-2, and 7 1-Hz MARK) and operated from October 2005 to March 2007. EGELADOS also consisted of seven permanent broadband seismographs that belonged to GeoForschungsNetz (GEOFON) network and one Mediterranean Very Broadband Seismographic Network (MedNet) station (Friederich and Meier, 2005). In addition to CYCNET and EGELADOS, seismicity along the Santorini-Amorgos zone is also monitored by the Hellenic Unified Seismic Network (HUSN). The HUSN permanent network was established in 2008 by merging the existing seismic networks in Greece. It consists of 153 stations equipped with 30–120-s three-component broadband seismometers (CMG-3ESPC, CMG-3 T, CMG-40 T, STS-1, STS-2, Le-3D, KS2000M, and TRILLIUM-120p) and was undergoing continuous development until 2011. Therefore, in this study we preferred to use HUSN data from 2011 to 2020.

Recently, Andinisari et al. (2021) utilized the NonLinLoc package (Lomax et al., 2000) and the 1D velocity model of Brüstle (2012) to obtain absolute locations of 1868 crustal events (M_L between 0.8 and 4.6) recorded by CYCNET (2002–2004), EGELADOS (2005–2007), and HUSN (2011–2019) along the Santorini-Amorgos zone (see Fig. 1). Here, we utilized the absolute locations published by Andinisari et al. (2021) and supplemented them with 14 absolute locations of HUSN events that occurred in the Santorini-Amorgos zone during 2020, resulting in 1882 absolute locations. The absolute locations of all these events are plotted in Fig. 2. Average horizontal (ERH) and vertical errors (ERV) of all these locations are 2.34 km ($\pm$ 5.15 km) and 3.08 km ($\pm$ 2.25 km), respectively. The distributions of RMS residual, azimuthal gap, ERH, and ERV of the located events are shown in Fig. S1 in the Supplementary Material. We also extracted the take-off angles, station azimuths, and epicentral distances of each event calculated by the NonLinLoc package. We further selected the events with azimuthal gaps less than 180°, having more than 5 P,S phase observation pairs and clear P-wave polarities,

yielding as many as 292 events that could potentially be used for moment tensor inversion.

3. Moment tensor inversion

3.1. Data preprocessing

The use of amplitude ratios to retrieve moment tensors required us to measure the amplitudes of P and S-wave first arrivals (P and S-phases). S-wave is recorded by two components with perpendicular motions to each other, namely SV and SH. While the amplitude of P-phase can easily be obtained from the vertical component, the amplitudes of SV and SH-phases can only be extracted from transverse and radial components. Therefore, the horizontal components have to be rotated into transverse and radial directions with respect to the epicenter of each event provided by NonLinLoc. After the seismogram rotations were performed, we low-pass filtered the three-component seismograms at 5 Hz. This filter was chosen for the reason that scattering is frequency dependent and strongly affects seismic waves of higher frequency bands, which is particularly true across the southern Aegean (Ranjan et al., 2019; Ranjan and Konstantinou, 2020). A comparison between original seismograms and rotated seismograms after low-pass filtering is displayed in Fig. 3.

We then corrected the three-component seismograms for attenuation and free-surface effects. Seismic waves are attenuated as they propagate due to energy loss and the heterogeneity of the Earth. The seismic wave attenuation of P and S-waves can be quantified by using the quality factors Q_P and Q_S that are directly related to the observed amplitudes of P-phase (A_p) and S-phase (A_s) as well as amplitudes of the P and S-phases at the source (A_{Po} and A_{So}) by using the following equation (Miller et al., 1998)

$$\frac{A_{Po}}{A_{So}} = \frac{A_P}{A_S}\frac{R_P}{R_S} \exp\left[\pi f_c t_p^* \left(1 - \left(\frac{Q_P}{Q_S}\right)\left(\frac{V_P}{V_S}\right)\right)\right] \tag{1}$$

where R_P and R_S are geometrical spreading factors for P and S-waves, f_c is the corner frequency used for seismogram filtering, and t_p^* is the whole-path attenuation operator for the P-wave. We employed the commonly used Q_P/Q_S value of 9/4 (Aki and Richards, 2002) and f_c of 5 Hz. We also utilized the average Vp/Vs ratio for Santorini, Kolumbo, and the area along the Santorini-Amorgos ridge (~1.81) estimated by Andinisari et al. (2021). Since there is no information regarding R_P and R_S, we considered that R_P/R_S is equal to 1 following Miller et al. (1998). The t_p^* for the depths of 0–25 km in southern Aegean is also not known, therefore a value of 0.03 is taken from the median value of t_p^* measured in eastern California for epicentral distances of 0–100 km (Hauksson and Shearer, 2006). By using the aforementioned values, the source amplitude ratio is represented as a function of the observed amplitude ratio as follows

$$\frac{A_{Po}}{A_{So}} = 0.23 \frac{A_P}{A_S} \tag{2}$$

Finally, we performed the correction for the free surface effect by following the method suggested by Kennett (1991).

3.2. Inversion methodology

Various methods have been developed to estimate the moment tensor of an earthquake by inverting its full waveforms, P-phase polarities, or amplitude ratios. The full waveform inversion is not feasible for events with Mw < 3 and the use of only P-wave polarities results in non-unique source mechanisms. Therefore, amplitude ratios are combined with the P-wave polarities in this study in order to better constrain the moment tensor solution. The use of amplitude ratios will simplify the inversion since we do not need to consider propagation effects and
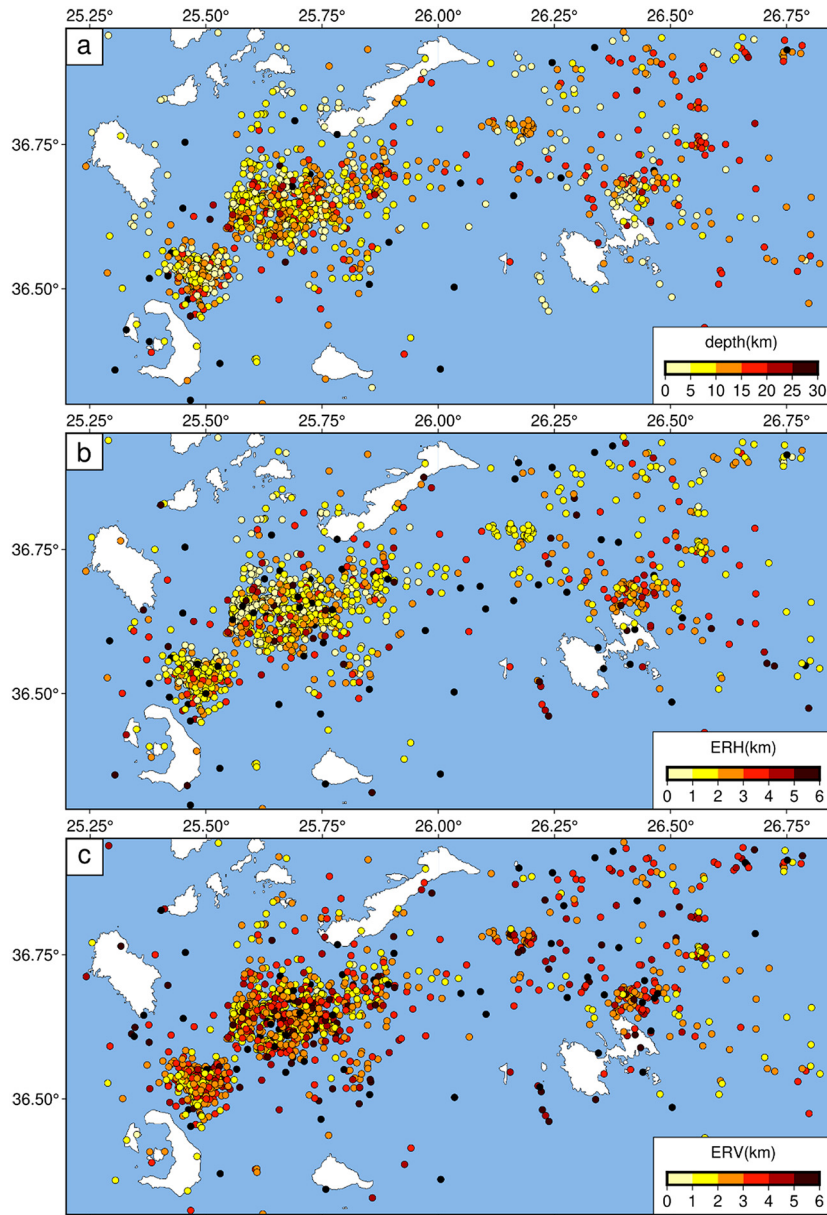
Fig. 2. Absolute locations of events taken from Andinisari et al. (2021) and of events throughout 2020 that occurred along the Santorini-Amorgos zone plotted as a function of (a) their hypocentral depths, (b) horizontal uncertainties (ERH), and (c) vertical uncertainties (ERV).

correction for event magnitude (Hardebeck and Shearer, 2003). An additional advantage of using amplitude ratios is that it cancels the instrument response contribution in the picked amplitudes. At the same time, however, it also transforms the moment tensor inversion into a nonlinear problem, which is computationally more expensive to solve (Jechumtálová and Šílený, 2005).

In this study, we used the amplitude ratios of SH/P and SV/P to determine the full moment tensor and constrain its sense of motion by using the P-wave polarities (e.g., Jechumtálová and Šílený, 2005). For stations with clear P-wave polarities and unclear SV and SH, we extracted the P-wave polarities only. We picked the amplitudes of P, SV, and SH waves in the rotated seismograms that have been corrected for attenuation and free-surface effects. We also used the values of take-off angles, station azimuths, and epicentral distances to estimate the synthetic P, SV, and SH amplitudes by using the Green's functions formulation described by Julian (1986). This calculation only utilized take-off angles with a quality score of 8–10 as assigned by NonLinLoc (0: poor quality, 10: best quality).

The observed P-wave polarity constraint can be expressed in the form of inequalities as

$$\mathbf{g}^{\mathrm{T}}\mathbf{m} \geq \mathbf{0} \text{ or } \mathbf{g}^{\mathrm{T}}\mathbf{m} \leq \mathbf{0} \tag{3}$$

where $\mathbf{g}$ is a column vector of six elements of the Green's function for a particular wave type (P or S), $\mathbf{m}$ is the vector containing six components of the moment tensor, and the symbol T represents matrix transposition. By using the inequalities described in Eq. (3) as constraints, the optimum moment tensor $\mathbf{m}$ can be estimated by iteratively performing minimization of the objective function F given by

$$F = \sum_{i \in S} \left| \mathbf{g}_i^{\mathrm{T}}\mathbf{m} - r_i \right| \tag{4}$$

where r indicates the observed amplitude ratio, i shows the index of the system of inequalities, and S is the set of polarity inequalities that constrain the sense of motion of the moment tensor solution.
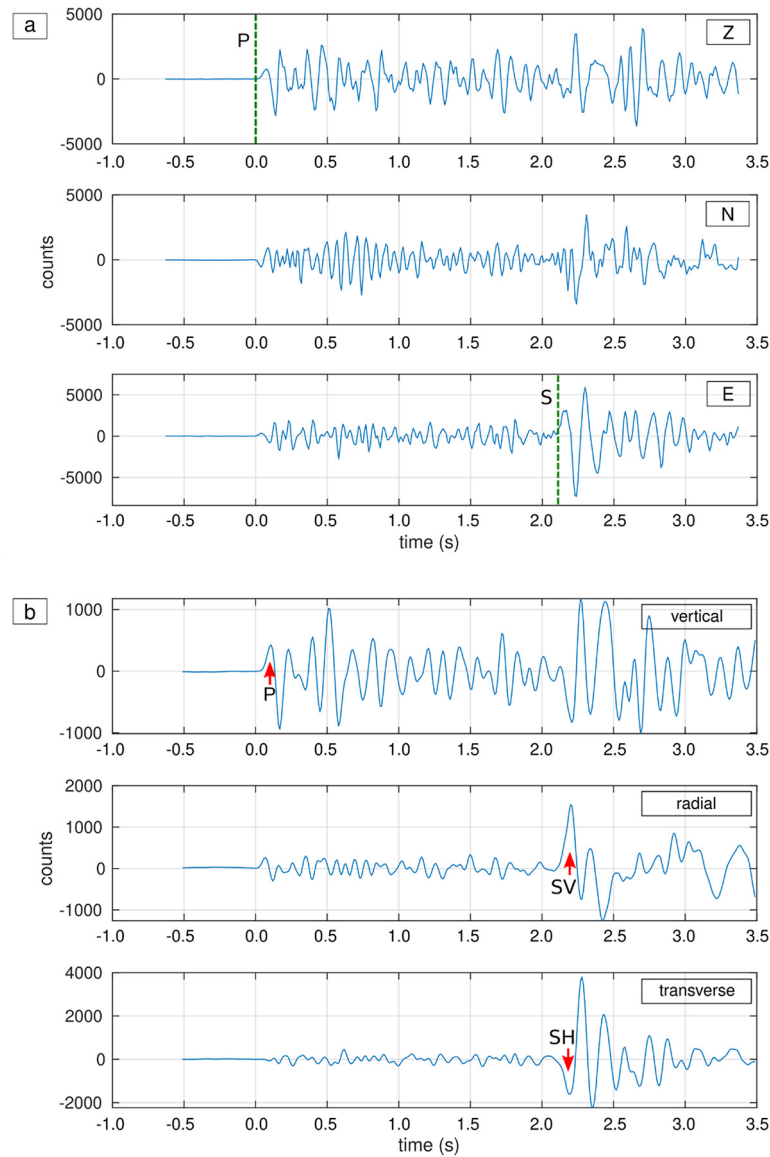
Fig. 3. Seismograms of an event recorded at station ANID on 1 May 2006 at 05:36:36 UTC. The seismograms in (a) are before rotation and filtering, and (b) are rotated and low-pass filtered at 5 Hz. The dashed green lines indicate P and S-wave arrivals. The red arrows represent the picks of P, SV, and SH amplitudes. (For interpretation of the references to colour in this figure legend, the reader is referred to the web version of this article.)

The minimization of the objective function in Eq. (4) was performed by using Sequential Quadratic Programming (SQP) (Nocedal and Wright, 2006). SQP is a method to estimate a numerical solution to non-linear optimization problems in several iterations by dividing the problem into constrained quadratic programming subproblems. In our case, the objective function will be modeled as a quadratic programming subproblem at its first iteration. Then, this subproblem is minimized (subject to the polarity constraint) to define the next iteration step and this routine is repeated until the minimization is completed. The quadratic subproblem has to be well determined so that it results in a good step for the nonlinear optimization problem in order for this approach to achieve convergence (Byrd et al., 1999). We used the 'sqp' function of GNU Octave in order to carry out the minimization in this study.

In order to determine the source mechanism of each event, the retrieved moment tensor is decomposed and rearranged to form the basic components. These basic components are the isotropic (ISO) that is characterized by positive or negative volume change, the double-couple (DC), and the compensated linear vector dipole (CLVD). We

calculated the percentage of moment tensor source components by using relative scale factors as proposed by Vavryčuk (2015). The results of the moment tensor decompositions and also the uncertainty of each component will be described in the following section.

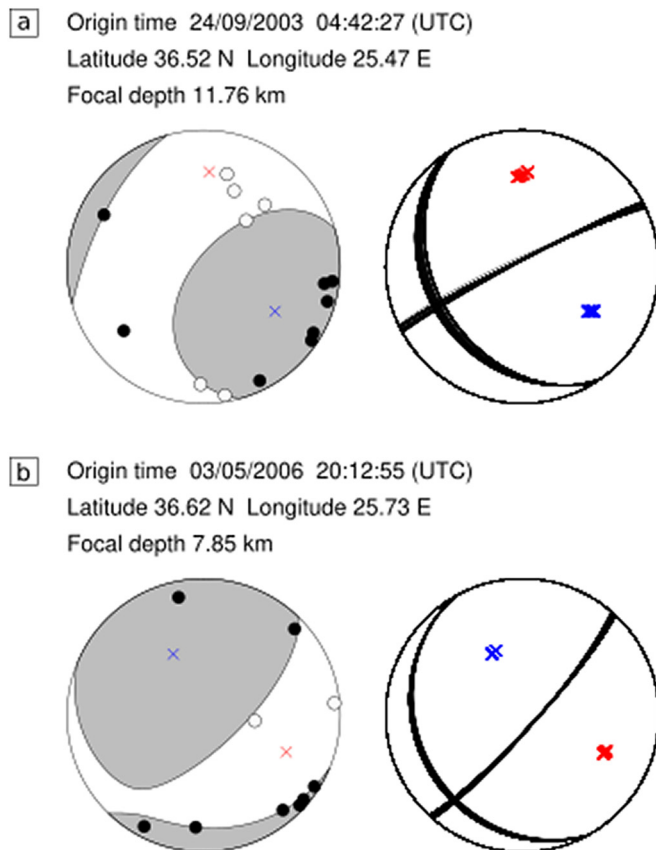### 3.3. Stability and characteristics of moment tensor solutions

We tested the stability of the retrieved moment tensors by adding random noise to the preprocessed seismograms with maximum values reaching 10% of the maximum amplitude of each waveform and constructed 200 noisy datasets for each event. Then, the moment tensor inversion and decomposition were performed for each of these datasets. We estimated the uncertainty of the moment tensors by using the sum of standard deviations (σ^{SUM}) of the ISO, CLVD, and DC components (σ^{ISO}, σ^{CLVD}, σ^{DC}) of the noisy datasets as previously done by Vavryčuk et al. (2008). We also made sure that the P/T-axes of the resulting moment tensors are well-clustered which is another indication of stable solutions.

Table 1
Parameters used to classify the moment tensors solutions of microearthquakes. N is the total number of P-polarities and P,S phase observation pairs used during the moment tensor inversion. The σ^{SUM} indicates the total uncertainties of DC, CLVD, and ISO.

Quality	N	Azimuthal gap	σ^{SUM} (%)	Polarity misfit
A	> 11	< 90°	< 10	0
B	6–11	90° – 160°	10–50	1–2
C	< 6	> 160°	> 50	> 2

The resulting moment tensors can be grouped into 3 quality classes based on the total number of P-polarities and P,S phase observation pairs, azimuthal gap, σ^{SUM}, and the number of polarities that are not in accordance with the sense of motion of the resulting moment tensor (polarity misfit). The selected thresholds of these parameters for each quality class are shown in Table 1. In this study, we only used the moment tensors of A and B-quality, yielding as many as 74 well-constrained moment tensor solutions. Fig. 4 shows examples of moment tensor solutions of events that occurred in Kolumbo and around Anydros island along with the P/T axes and nodal planes obtained from the inversion of the noisy datasets. The rest of the well-constrained moment tensors are plotted in Fig. S2 in the Supplementary Material. The complete moment tensor elements as well as the values of strike, dip, and rake of all the events can be found in Table S1 in the Supplementary Material, while the results of moment tensors decomposition are presented in Table S2 in the Supplementary Material. The inverted events in this

study have an average azimuthal gap of 99.5° and are observed by at least 6 seismic stations. The average standard deviations for the DC component is 3.3%, while the average standard deviations for the non-DC components are 3.3% for the CLVD and 1.2% for the ISO. Based on these uncertainties, we can conclude that the bulk of the non-DC components is not due to artefacts caused by the inversion.
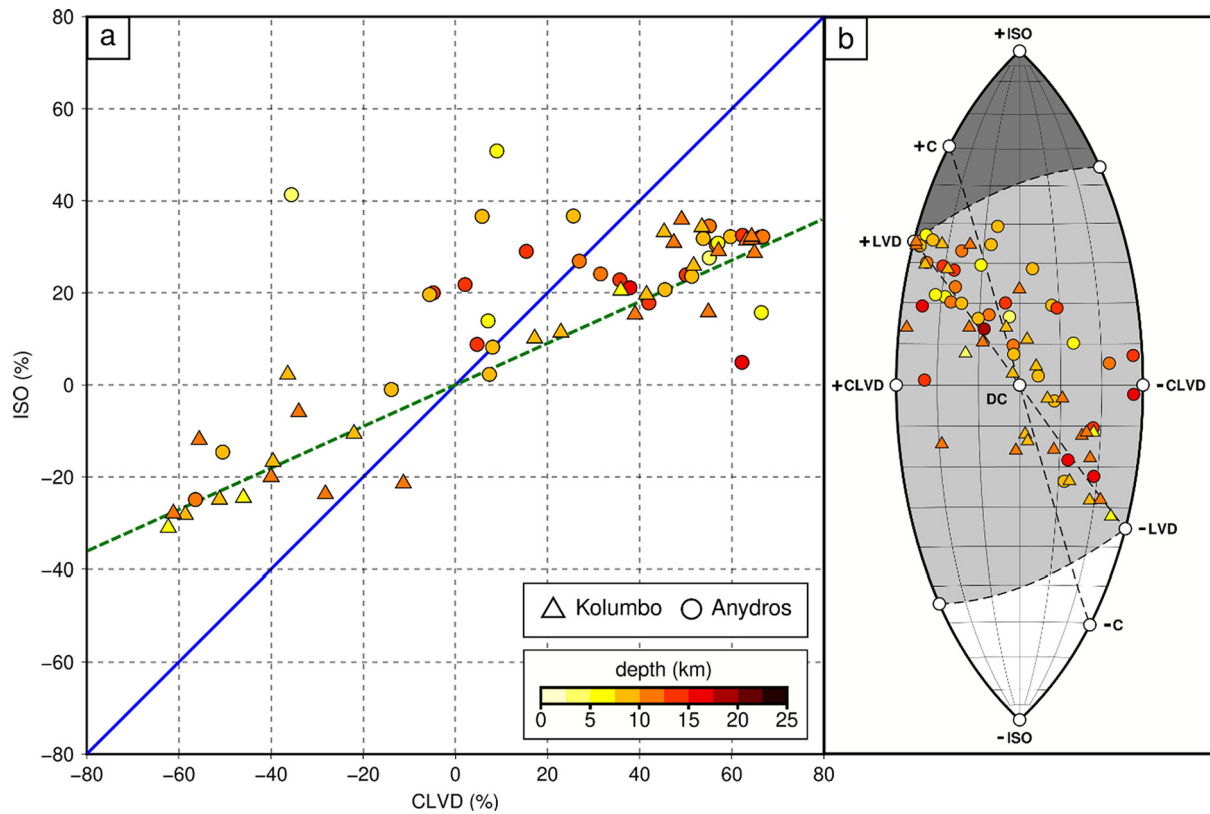
The CLVD and ISO components of our moment tensors are found to be possitively correlated with the coefficient of determination R^2 equal to 0.68 as shown in the left panel diagram of Fig. 5. From this diagram, we can also see that most of the moment tensors found in Anydros have positive non-DC components, while the ones in Kolumbo have similar number of events with positive and negative non-DC components. In order to visualize the source components of all the events, we plotted the retrieved moment tensors into the Lune diagram of Tape and Tape (2013) as seen in the right panel diagram of Fig. 5. The Lune diagram is a source-type plot where every data point projected into it represents a moment tensor solution. The vertical axis of the Lune indicates the isotropic axis, while the horizontal axis indicates the deviatoric plane. By plotting moment tensor solutions into the Lune, we basically organized them based on their eigenvalues. The dark grey shaded area in the upper part of the Lune indicates the area where moment tensors have all positive eigenvalues, while the white shaded area at the bottom indicates the opposite. Moment tensors that are projected into these mentioned areas are mostly generated by explosion or implosion. On the other hand, moment tensor solutions that fall into the grey area in the central part of the Lune have both positive and negative eigenvalues. From the Lune, we can see that most of the moment tensors in our study areas fall roughly along the dashed line connecting the extensive and compressive LVD (linear vector dipole). The LVD itself is a mechanism similar to CLVD, but with larger volumetric expansion or compression. Furthermore, a small number of events that occurred in Kolumbo and Anydros also seem to have significant DC components, while there are no events that exhibit dominant ISO component related to explosion or implosion. From the diagrams in Fig. 5, it can be concluded that the resultant source of the majority of events in our study area is a combination of positively correlated non-DC components with a small percentage of DC component.

4. Discussion

4.1. Possible causes of non-DC components

One possible source of the non-DC component may be multiple shear faulting or complex rupture that involves a combination of fault segments with various orientations. A mechanism caused by the combination of two or more shear faulting sources will be able to produce a CLVD component, but this mechanism cannot generate a volumetric change resulting in a vanishing ISO component (Julian et al., 1998). Since the moment tensors in this study have significant ISO components (−31.0% to 50.8%), multiple or complex shear faulting is less likely responsible for the observed non-DC components. Moreover, the magnitude of events that occurred along the Santorini-Amorgos zone is small with the majority of events having local magnitude of less than 3, that are less likely to have been caused by multiple shear faulting or complex rupture.

Anisotropy is also a possible cause of earthquakes with large non-DC components since it affects the polarization, velocity, and amplitudes of the propagating seismic wave (Vavryčuk et al., 2008). Anisotropy also affects the relation of the fault geometry and its moment tensor representation. A recent study by Konstantinou et al. (2021) estimated the percentage of crustal anisotropy across the southern Aegean by measuring the shear wave splitting of 5194 earthquakes. The average value of anisotropy in the Santorini-Amorgos zone, measured at 16 seismic stations (see Fig. 1) along the region, is found to be 1.25%. This low percentage of anisotropy indicates that the crust consists of rocks that are not heavily fractured and may be considered to first order as isotropic

[a] Origin time 24/09/2003 04:42:27 (UTC)
Latitude 36.52 N Longitude 25.47 E
Focal depth 11.76 km

[b] Origin time 03/05/2006 20:12:55 (UTC)
Latitude 36.62 N Longitude 25.73 E
Focal depth 7.85 km

Fig. 4. Example of moment tensor solutions of events that occurred (a) beneath Kolumbo and (b) near the island of Anydros. Moment tensor solutions in the left panel depict the retrieved best fit moment tensors. Moment tensor solutions in the right panel show nodal planes of the DC part of the 200 noisy datasets (see text for more details). The black and white circles indicate stations with positive and negative P-polarities, respectively. The blue cross represents T-axis, while red cross represents P-axis. (For interpretation of the references to colour in this figure legend, the reader is referred to the web version of this article.)

Fig. 5. Diagrams depicting the decomposed source components of the moment tensors. (a) Diagram indicating the correlation of CLVD and ISO components of moment tensors in Kolumbo and around the island of Anydros. Blue line has a slope of 1 which represents perfect correlation between the ISO and CLVD components. Dashed green line shows the linear trend line of ISO and CLVD components with coefficient of determination R^2 equal to 0.68. (b) The Lune diagram showing the source components of the moment tensors. The colour of the symbols indicates the hypocentral depth as shown in the colour scale in (a). (For interpretation of the references to colour in this figure legend, the reader is referred to the web version of this article.)

(Crampin and Peacock, 2008). Moreover, the presence of anisotropy would likely result in events with uncorrelated ISO and CLVD components (Vavryčuk, 2015) unlike the retrieved moment tensors. Hence, anisotropy is probably not the main cause for the non-DC components that we observe in our study area.

Another possible origin of non-DC components is tensile faulting due to high pore pressure. High pore pressure along a fault during rupture will result in either tensile faulting or a combination of shear and tensile faulting, generating an event commonly known as tensile earthquake (Vavryčuk et al., 2008; Vavryčuk, 2011). This earthquake is characterized by significant CLVD and ISO components that are positively correlated to each other. Considering the existence of fluids along the Santorini-Amorgos zone (Andinisari et al., 2021) and also the fact that the non-DC components are mostly positively correlated, tensile faulting owing to high pore pressure is the most likely mechanism for the non-DC components in our study area.

Several studies of moment tensor inversion at volcanic and geothermal areas have been performed by using similar inversion methodology as ours, such as in the Hengill–Grensdalur volcanic complex, Iceland (Miller et al., 1998), Long Valley caldera, California (Foulger et al., 2004), and the Geysers geothermal reservoir in California (Martínez-Garzón et al., 2013). The retrieved moment tensors exhibited significant non-DC components which were probably caused by a combination of shear and tensile faulting due to fluid flow. The resulting non-DC components in these studies consist of significant CLVD part, ranging from −88.5% to 83.8%, and slightly lower isotropic part, ranging from −44.0% to 71.6%. The inverted moment tensor solutions in Kolumbo and Anydros, with CLVD from −62.3% to 81.8% and isotropic part from −31.0% to 50.8%, are within the range observed in the aforementioned areas. In all the aforementioned studies, the presence of fluids is an

important factor in causing earthquakes with significant non-DC components, which is also very likely to be occurring in our study area. A lune diagram comparison between the moment tensors in our study and each of the areas mentioned above is shown in Fig. S3 in the Supplementary Material.

We plotted the moment tensor solutions based on the sign (positive or negative) of their non-DC components along with the precise relative locations of microseismicity from Andinisari et al. (2021) in Fig. 6. These locations were obtained by using the double-difference algorithm (HypoDD) and the 1D velocity model of Brüstle (2012), resulting in precise relative locations with horizontal and vertical uncertainties of less than 0.3 km. There are 32 and 34 moment tensors found beneath Kolumbo and around Anydros (within a radius of ~10 km) respectively. As many as 8 well-constrained moment tensors are also found outside the mentioned areas, one of them in close proximity to the Santorini-Anafi fault (SAF). The moment tensor solutions found in Kolumbo and Anydros as well as their relation with the seismicity distribution and tectonic setting will be discussed in the following subsections.

4.2. Kolumbo submarine volcano

Kolumbo submarine volcano is the largest among the volcanic craters in the area and is located about 7 km NE of Santorini caldera. The closest major normal faults to Kolumbo are Ios and Anydros faults, which are located to its NW and SE, respectively (Fig. 7). It has been previously suggested that these faults control the volcanic activities of Kolumbo (Sakellariou et al., 2010). However, the relocated seismicity does not appear to be related to any of these faults (Andinisari et al., 2021). The smaller volcanic craters in the area are aligned to NNE and NE with respect to Kolumbo, in accordance with the orientation of the
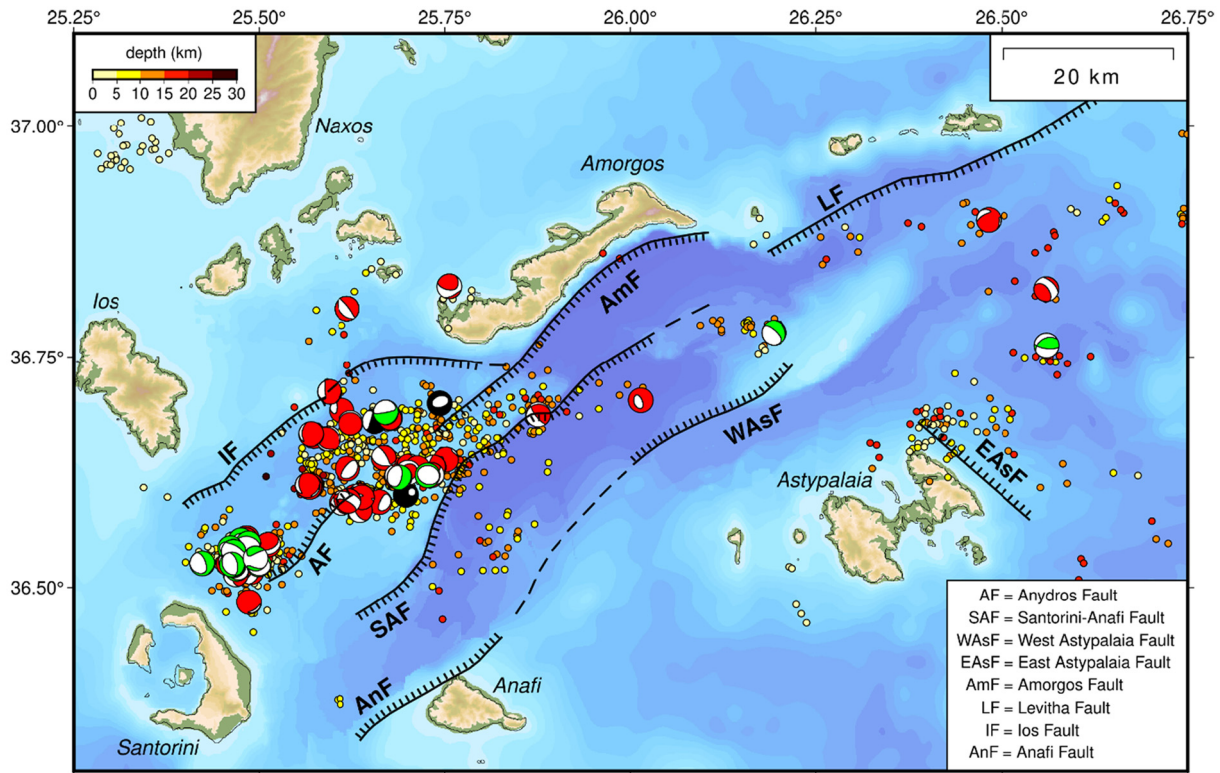
Fig. 6. The resulting moment tensors and relative locations of events taken from Andinisari et al. (2021) along the Santorini-Amorgos zone. The green moment tensor solutions indicate events with negative non-DC components, while the red moment tensor solutions indicate events with positive non-DC components. The black moment tensor solutions correspond to events with negative CLVD and positive ISO components or the opposite. The colour of every small circle represents a depth value based on the scale at the upper left. The comb-like black lines indicate major normal fault traces investigated by Perissoratis and Papadopoulos (1999), Nomikou et al. (2018), and also fault traces found in the GreDaSS database (Caputo and Pavlides, 2013). (For interpretation of the references to colour in this figure legend, the reader is referred to the web version of this article.)

major faults along the Santorini-Amorgos zone. The dominant features of Kolumbo and these smaller volcanic craters are the faulting and fracturing that reflect the influence of extensional tectonic processes (Nomikou et al., 2012). Dimitriadis et al. (2009) found that the local extensional axis at Kolumbo deviates ~30° counter clockwise with respect to the prevailed NW-SE extensional axis of the Santorini-Amorgos zone. Andinisari et al. (2021) estimated the petrophysical parameters along the Santorini-Amorgos zone by utilizing travel time data of crustal earthquakes with maximum hypocentral depth of 25 km. Therefore, the resulting parameter values can be considered as the averaged values for the whole crust. The authors found that the Vp/Vs ratios for the Kolumbo area is in the range of 1.77–1.82, while the Poisson's ratio varies from 0.26 to 0.28. From the range of Vp/Vs ratios, we can conclude that magmatic fluids are likely present in the area, including a fraction of CO_2. The Poissons's ratios also indicate that this area is mostly characterized by partially saturated cracks. The authors also suggested that the observed microseismicity beneath Kolumbo may be caused by the movement of melt from a deep reservoir to the shallow magma chamber at the depth of 6–7 km.

Fig. 7 is the map of 32 moment tensors beneath Kolumbo along with the Frohlich diagrams (Frohlich, 1992) and the corresponding cross-sections. The events here occurred at depths of 5.8–12.2 km, with the component percentages in the ranges of 3.5% to 72.8%, −62.3% to 81.8%, and − 31.0% to 35.9% for DC, CLVD, and ISO, respectively. The maximum uncertainty of all the components is σ^{SUM} of 45.7%. The majority of events in this area fall under the category of pure normal and oblique faults as shown in the Frohlich diagram in the inset of Fig. 7. Deviation of local extensional axis as observed in this area is often accompanied by a drastic change in faulting pattern from normal to oblique fault (Dimitriadis et al., 2009). However, this is not the case for Kolumbo as both normal and oblique faults are present here.

The cross-sections a-a' to e-e' in Fig. 7 show that most of the reliable moment tensors beneath Kolumbo are subvertical CLVD with a deviation of ~21° from the vertical. We can also see that moment tensors with positive (red moment tensor solutions in Fig. 7) and negative non-DC components (green moment tensor solutions in Fig. 7) beneath Kolumbo are almost similar in number. Additionally, we can also observe that most of the moment tensors with negative non-DC components are found at shallower depths of less than 11 km compared to those with positive non-DC components. It is possible that a steady upward migration of magmatic fluids from the deep reservoir to the shallow magma chamber is causing the opening and closing of the subvertical cracks beneath the magma chamber. The moment tensors with negative non-DC components that are found at the shallower depths may be caused by the closing of cracks as the fluids move into the chamber. The whole process generates events with positive and negative non-DC components that are projected as the subvertical CLVDs shown in the cross-sections of Fig. 7. The opening and closing of cracks due to upward fluids migration also explains the source of small magnitude earthquake clusters observed beneath the magma chamber of Kolumbo (see cross-section e-e' in Fig. 7). The possibility of upward fluids migration beneath Kolumbo is also consistent with the values of petrophysical parameters estimated by Andinisari et al. (2021). All of these observations show that fluids have an important role in causing the seismicity observed beneath Kolumbo.

4.3. Anydros island

In general, the Santorini-Amorgos zone is characterized by crustal weakness due to the extensional deformation in the NW-SE direction, creating overlapping NE-SW oriented normal fault segments as well as multiple basins and ridges. The small island of Anydros is located at
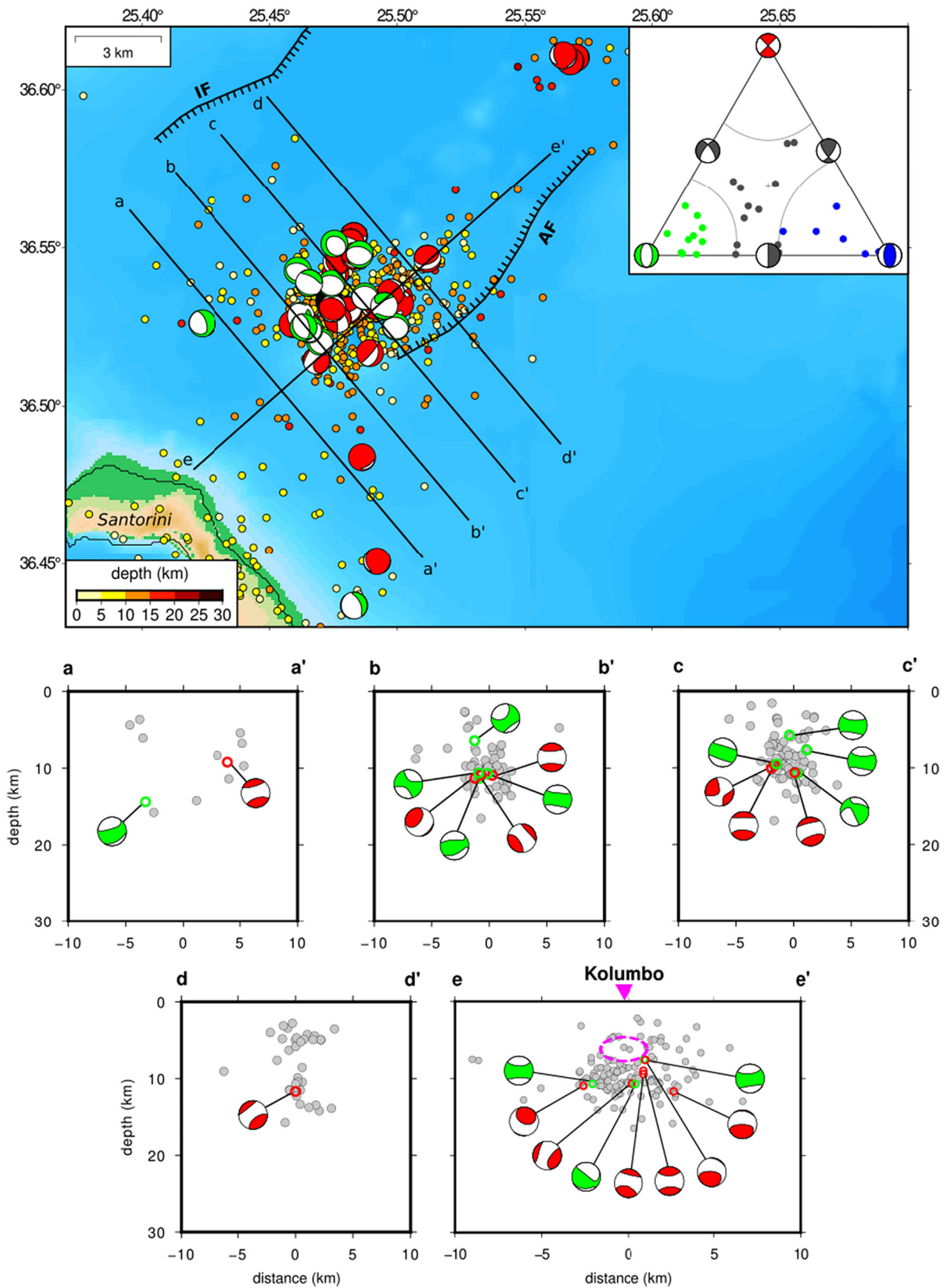
Fig. 7. The relative locations and moment tensors of events beneath Kolumbo and the corresponding Frohlich diagram. The fractions of normal, strike-slip, and thrust fault for the DC components of the best fits are depicted in the Frohlich diagram in the inset. The black solid lines correspond to the cross sections in the lower panel. The dashed magenta ellipse in cross-section e-e' depicts the location of Kolumbo magma chamber (Dimitriadis et al., 2010; Cantner et al., 2014). (For interpretation of the references to colour in this figure legend, the reader is referred to the web version of this article.)
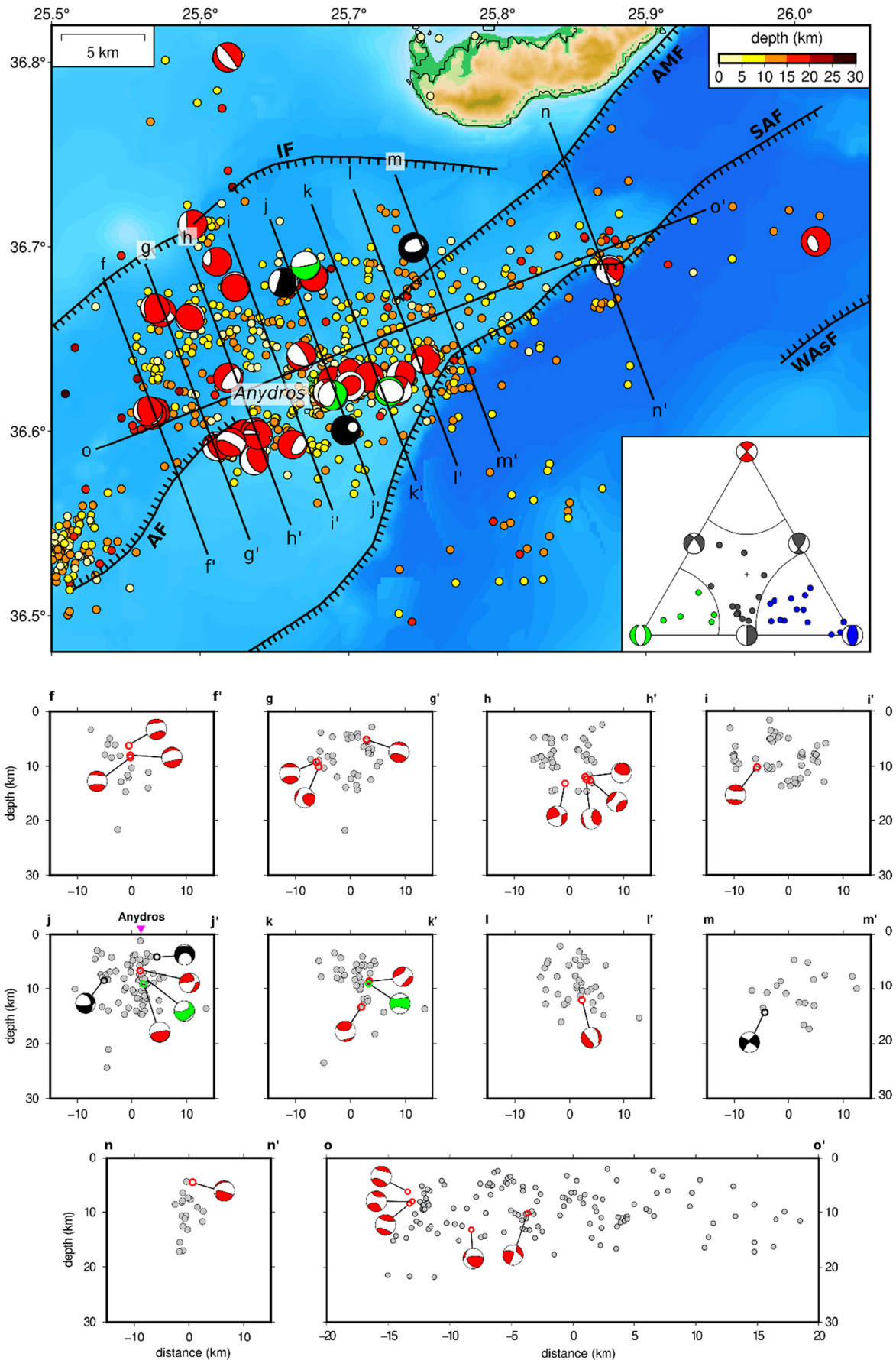
Fig. 8. The relative locations and moment tensors of events around the island of Anydros and the corresponding Frohlich diagrams. All other symbols are the same as in Fig. 7.

the highest part of the Santorini-Amorgos ridge, at the boundary area that separates Anydros and Santorini-Anafi basins (Nomikou et al., 2018). Swath bathymetry data shows that the Amorgos-Anydros-Anafi region, including the area around Anydros, experienced extreme changes in seafloor topography, which may be related to deformation and volcanism (Hooft et al., 2017). Vertical earthquake clusters were observed beneath Anydros and beneath the NE segment of Santorini-Amorgos fault (Bohnhoff et al., 2006; Andinisari et al., 2021). The area around Anydros is associated with the Vp/Vs ratios in the range of 1.72–1.80 and Poisson's ratios of 0.25–0.28 (Andinisari et al., 2021). Compared to the petrophysical parameters of Kolumbo, the Vp/Vs ratios and Poisson's ratios in this area exhibit slightly lower values. Even so, the maximum Vp/Vs and Poisson's ratios found here still indicate the presence of fluids and partially saturated cracks.

We plotted the 34 events with well-constrained moment tensors around the island of Anydros along with the Frohlich diagram and the corresponding cross-sections in Fig. 8. The moment tensors we present here are inverted from events with hypocentral depths of 4.0–17.3 km. The DC components of these events ranged from 1.1% to 90.4%, while the CLVD and ISO components are in the ranges of −56.4% to 66.7% and − 24.9% to 50.8%, respectively, with the maximum σ^{SUM} of this area is 33.2%. As we can see in the Frohlich diagram in Fig. 8, most of the focal mechanisms of events around Anydros are categorized as thrust and various oblique faults, while only five are characterized as normal faults.

Events with dominant non-DC components are associated with subvertical CLVD mechanisms with a deviation of ~30° from the vertical axis, as seen in cross-sections f-f', g-g', i-i', n-n', and o-o'. All of the subvertical CLVD shown in these cross-sections are associated with positive non-DC components, which signify that most of the events that occurred in the region may be caused by the opening of cracks. It could be that the extensional deformation in the area and high pore fluid pressure open subvertical cracks that facilitate the ascent of magmatic fluids from a greater depth. This possibility is supported by the existence of vertical earthquake clusters that were imaged by Bohnhoff et al. (2006) and Andinisari et al. (2021) beneath the island of Anydros and beneath the NE segment of Santorini-Amorgos zone (see cross-sections j-j' and n-n' in Fig. 8). These vertical earthquake clusters are also related to subvertical CLVD mechanisms, especially the one observed beneath the NE segment of Santorini-Amorgos fault, and may serve as pathways that facilitate fluids to the surface. This confirms the suggestion of Andinisari et al. (2021) that magmatic fluids exist in this region and that the rocks are partially saturated with fluids.

5. Conclusions

We performed moment tensor inversion of P-wave polarities and SV/P, SH/P amplitude ratios for microearthquakes recorded by temporary and permanent networks, yielding 74 well-constrained moment tensor solutions. The derived moment tensors are sufficient to highlight the areas of interest in Santorini-Amorgos zone, which are the Kolumbo submarine volcano and the area around the small island of Anydros. These moment tensors have CLVD and ISO components with percentages that ranged from −62.3% to 81.8% and − 31.0% to 50.8%, respectively. Since these non-DC components are positively correlated, tensile faulting is the most likely cause of the microseismicity in the study area. The positive and negative non-DC components observed in Kolumbo are most likely generated by the opening and closing of cracks beneath the shallow magma chamber due to a steady migration of magmatic fluids from the deep reservoir into the chamber as shown in the cartoon of fluids-crack interaction in Fig. 9a. In Anydros, most of the microearthquakes have positive non-DC components associated with the opening of cracks. It is possible that the extensional deformation in the area and high pore fluid pressure open subvertical cracks that facilitate the ascent of magmatic fluids from the greater depth as shown in Fig. 9b. The upward migration of magmatic fluids at Anydros combined with the extensional regime of the Santorini-Amorgos zone can be considered as an indication of emerging volcanic activity in this area.
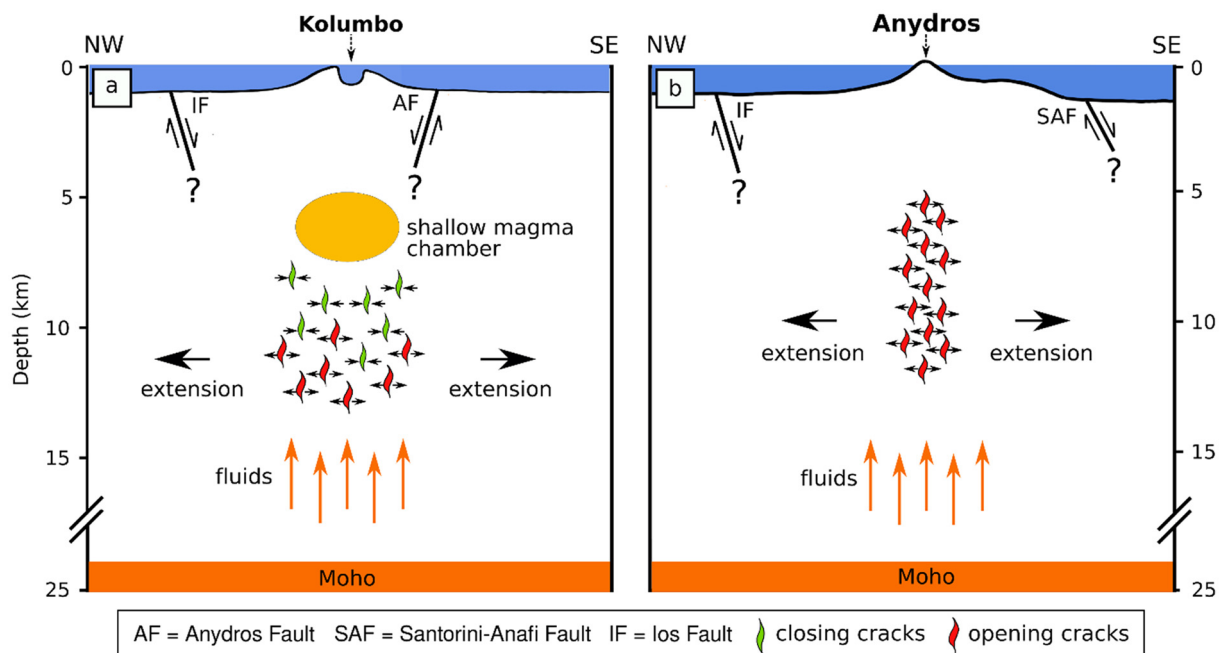
Fig. 9. Cartoon illustrating the fluids-crack interaction in our study area. (a) In Kolumbo, upward migration of fluids from the deep reservoir to the shallow magma chamber open and close the subvertical cracks beneath the magma chamber. (b) Around the small island of Anydros, extensional deformation and high pore fluid pressure open subvertical cracks which are subsequently filled by the ascending fluids. The question marks indicate that the faults extend to unknown depths.

Supplementary data to this article can be found online at https://doi.org/10.1016/j.jvolgeores.2021.107394.

Funding

Declaration of Competing Interest

The authors declare that they have no known competing financial interests or personal relationships that could have appeared to influence the work reported in this paper.

Acknowledgements

References

Aki, K., Richards, P., 2002. Quantitative Seismology. 2nd edition. University Science Books, Sausalito.

Andinisari, R., Konstantinou, K.I., Ranjan, P., 2021. Seismicity along the Santorini-Amorgos zone and its relationship with active tectonics and fluid distribution. Phys. Earth Planet. Inter., 106660 https://doi.org/10.1016/j.pepi.2021.106660.

Bohnhoff, M., Rische, M., Meier, T., Endrun, B., Harjes, H.-P., Stavrakakis, G., 2004. A temporary seismic network on the Cyclades (Aegean Sea, Greece). Seismol. Res. Lett. 75 (3), 352–357. https://doi.org/10.1785/gssrl.75.3.352.

Bohnhoff, M., Rische, M., Meier, T., Becker, D., Stavrakakis, G., Harjes, H.P., 2006. Microseismic activity in the Hellenic Volcanic Arc, Greece, with emphasis on the seismotectonic setting of the Santorini Amorgos Zone. Tectonophysics 423 (1–4), 17–33. https://doi.org/10.1016/j.tecto.2006.03.024.

Brüstle, A., 2012. Seismicity of the Eastern Hellenic Subduction Zone. Ph.D. thesisRuhr University, Bochum.

Byrd, R.H., Hribar, M.E., Nocedal, J., 1999. An Interior Point Algorithm for Large-Scale Nonlinear programming. SIAM J. Optim. 9 (4), 877–900.

Cantner, K., Carey, S., Nomikou, P., 2014. Integrated volcanologic and petrologic analysis of the 1650AD eruption of Kolumbo submarine volcano, Greece. J. Volcanol. Geotherm. Res. 269, 28–43. https://doi.org/10.1016/j.jvolgeores.2013.10.004.

Caputo, R., Pavlides, S., 2013. The Greek Database of Seismogenic Sources (GreDaSS), Version 2.0.0: A Compilation of Potential Seismogenic Sources (Mw & 5.5) in the Aegean Region. https://doi.org/10.15160/unife/gredass/0200. http://gredass.unife.it/.

Carey, S., Nomikou, P., Bell, K.C., Lilley, M., Lupton, J., Roman, C., Stathopoulou, E., Bejelou, K., Ballard, R., 2015. CO₂ degassing from hydrothermal vents at Kolumbo submarine volcano, Greece, and the accumulation of acidic crater water. Geology 41 (9), 1035–1038. https://doi.org/10.1130/G34286.1.

Crampin, S., Peacock, S., 2008. A review of the current understanding of seismic shearwave splitting in the Earth's crust and common fallacies in interpretation. Wave Motion 45, 675–722. https://doi.org/10.1016/j.wavemoti.2008.01.003.

Dimitriadis, I., Karagianni, E., Panagiotopoulos, D.G., Papazachos, C., Hatzidimitriou, P., Bohnhoff, M., Rische, M., Meier, T., 2009. Seismicity and active tectonics at Coloumbo Reef (Aegean Sea, Greece): monitoring an active volcano at Santorini Volcanic Center using a temporary seismic network. Tectonophysics 465, 136–149. https://doi.org/10.1016/j.tecto.2008.11.005.

Dimitriadis, I., Papazachos, C., Panagiotopoulos, D., Hatzidimitriou, P., Bohnhoff, M., Rische, M., Meier, T., 2010. P and S velocity structures of the Santorini-Coloumbo volcanic system (Aegean Sea, Greece) obtained by non-linear inversion of travel times

and its tectonic implications. J. Volcanol. Geotherm. Res. 195 (1), 13–30. https://doi.org/10.1016/j.jvolgeores.2010.05.013.

Foulger, G.R., Julian, B.R., Hill, D.P., Pitt, A.M., Malin, P.E., Shalev, E., 2004. Non-double-couple microearthquakes at Long Valley caldera, California, provide evidence for hydraulic fracturing. J. Volcanol. Geotherm. Res. 132-1, 45–71. https://doi.org/10.1016/S0377-0273(03)00420-7.

Friederich, W., Meier, T., 2005. EGELADOS project 2005/07, RUB Bochum, Germany. Deutsches GeoForschungsZentrum GFZ. https://doi.org/10.14470/m87550267382.

Friedrich, W.L., 2013. The Minoan Eruption of Santorini around 1613 B.C. and its consequences. Tagungen des Landesmuseums für Vorgeschichte Halle 9, 37–48.

Frohlich, C., 1992. Triangle diagrams: ternary graphs to display similarity and diversity of earthquake focal mechanisms. Phys. Earth Planet. Inter. 75, 193–198. https://doi.org/10.1016/0031-9201(92)90130-N.

Guilhem, A., Hutchings, L., Dreger, D.S., Johnson, L.R., 2014. Moment tensor inversions of M~3 earthquakes in the Geysers geothermal fields, California. J. Geophys. Res. Solid Earth 119, 2121–2137. https://doi.org/10.1002/2013JB010271.

Hardebeck, J.L., Shearer, P.M., 2003. Using S/P amplitude ratios to constrain the focal mechanisms of small earthquakes. Bull. Seismol. Soc. Am. 93 (6), 2434–2444. https://doi.org/10.1785/0120020236.

Hauksson, E., Shearer, P.M., 2006. Attenuation models (QP and QS) in three dimensions of the southern California crust: Inferred fluid saturation at seismogenic depths. J. Geophys. Res. 111, B05302. https://doi.org/10.1029/2005JB003947.

Hollenstein, C., Müller, M.D., Geiger, A., Kahle, H.-G., 2008. Crustal motion and deformation in Greece from a decade of GPS measurements, 1993–2003. Tectonophysics 449 (1), 17–40. https://doi.org/10.1016/j.tecto.2007.12.006.

Hooft, E.E.E., Nomikou, P., Toomey, D.R., Lampridou, D., Getz, C., Christopoulou, M.E., O'Hara, D., Arnoux, G.M., Bodmer, M., Gray, M., Heath, B.A., VanderBeek, B.P., 2017. Backarc tectonism, volcanism, and mass wasting shape seafloor morphology in the Santorini-Christiana-Amorgos region of the Hellenic Volcanic Arc. Tectonophysics 712–713, 396–414. https://doi.org/10.1016/j.tecto.2017.06.005.

Hübscher, C., Ruhnau, M., Nomikou, P., 2015. Volcano-tectonic evolution of the polygenetic Kolumbo submarine volcano/Santorini (Aegean Sea). J. Volcanol. Geotherm. Res. 291, 101–111. https://doi.org/10.1016/j.jvolgeores.2014.12.020.

Jechumtálová, Z., Šílený, J., 2005. Amplitude ratios for complete moment tensor retrieval. Geophys. Res. Lett. 32, L22303. https://doi.org/10.1029/2005GL023967.

Julian, B.R., 1986. Analysing seismic-source mechanisms by linear-programming methods. Geophys. J. Int. 84 (2), 431–443. https://doi.org/10.1111/j.1365-246X.1986.tb04364.x.

Julian, B.R., Miller, A.D., Foulger, G.R., 1998. Non-double-couple earthquakes 1. Theory Rev. Geophys. 36 (4), 525–549. https://doi.org/10.1029/98RG00716.

Kennett, B.L.N., 1991. The Removal of free surface interactions from three-component seismograms. Geophys. J. Int. 104, 153–154. https://doi.org/10.1111/j.1365-246X.1991.tb02501.x.

Klaver, M., Carey, S., Nomikou, P., Smet, I., Godelitsas, A., Vroon, P., 2016. A distinct source and differentiation history for Kolumbo submarine volcano, Santorini volcanic field, Aegean arc. Geochem. Geophys. Geosyst. 17, 3254–3273. https://doi.org/10.1002/2016GC006398.

Konstantinou, K.I., 2020. Magma chamber evolution during the 1650 AD Kolumbo eruption provides clues about past and future volcanic activity. Sci. Rep. 10, 15423. https://doi.org/10.1038/s41598-020-71991-y.

Konstantinou, K.I., Evangelidis, C.P., Liang, W.-T., Melis, N.S., Kalogeras, I., 2013. Seismicity, Vp/Vs and shear wave anisotropy variations during the 2011 unrest at Santorini caldera, southern Aegean. J. Volcanol. Geotherm. Res. 267, 57–67. https://doi.org/10.1016/j.jvolgeores.2013.10.001.

Konstantinou, K.I., Syahra, V., Ranjan, P., 2021. Crustal anisotropy in the southern Aegean from shear wave splitting of local earthquakes. J. Geodyn. 143. https://doi.org/10.1016/j.jog.2020.101810.

Křížová, D., Zahradník, J., Kiratzi, A., 2013. Resolvability of isotropic component in regional seismic moment tensor inversion. Bull. Seismol. Soc. Am. 103 (4), 2460–2473. https://doi.org/10.1785/0120120097.

Le Pichon, X., Chamot-Rooke, N., Lallemant, S., Noomen, R., Veis, G., 1995. Geodetic determination of the kinematics of Central Greece with respect to Europe: implications for eastern Mediterranean tectonics. J. Geophys. Res. 100 (B7), 12,675–12,690. https://doi.org/10.1029/95JB00317.

Lomax, A., Virieux, J., Volcant, P., Thierry-Berge, C., 2000. Probabilistic earthquake location in 3D and layered models. In: Thurber, C.H., Rabinowitz, N. (Eds.), Advances is Seismic Events Location, pp. 101–134 Amsterdam.

Martínez-Garzón, P., Bohnhoff, M., Kwiatek, G., Dresen, G., 2013. Stress tensor changes related to fluid injection at the Geysers geothermal field, California. Geophys. Res. Lett. 40, 2596–2601. https://doi.org/10.1002/grl.50438.

McClusky, S., Balassanian, S., Barka, A., Demir, C., Ergintav, S., Georgiev, I., Gurkan, O., Hamburger, M., Hurst, K., Kahle, H., Kastens, K., Kekelidze, G., King, R., Kotzev, V., Lenk, O., Mahmoud, S., Mishin, A., Nadariya, M., Ouzounis, A., Paradissis, D., Peter, Y., Prilepin, M., Reilinger, R., Sanli, I., Seeger, H., Tealeb, A., Toksöz, M.N., Veis, G., 2000. Global positioning system constraints on plate kinematic and dynamics in the eastern Mediterranean and Caucasus. J. Geophys. Res. 105, 5695–5719. https://doi.org/10.1029/1999JB900351.

Miller, A.D., Julian, B.R., Foulger, G.R., 1998. Three-dimensional seismic structure and moment tensors of non-double-couple earthquakes at the Hengill–Grensdalur volcanic complex, Iceland. Geophys. J. Int. 133 (2), 309–325. https://doi.org/10.1046/j.1365-246X.1998.00492.x.

Nocedal, J., Wright, S.J., 2006. Numerical Optimization. Second edition. Springer Series in Operations Research, Springer Verlag.

Nomikou, P., Carey, S., Papanikolaou, D., Croff Bell, K., Sakellariou, D., Alexandri, M., Bejelou, K., 2012. Submarine volcanoes of the Kolumbo volcanic zone NE of Santorini

Caldera, Greece. Glob. Planet. Chang. 90–91, 135–151. https://doi.org/10.1016/j.gloplacha.2012.01.001.

Nomikou, P., Papanikolaou, D., Pyle, D.M., Mather, T.A., Carey, S., Watts, A.B., Paulatto, M., Kalnins, M.L., Livanos, I., Bejelou, K., Simou, E., Perros, I., 2014. The emergence and growth of a submarine volcano: the Kameni islands, Santorini (Greece). GeoResJ 1–2, 8–18. https://doi.org/10.1016/j.grj.2014.02.002.

Nomikou, P., Hübscher, C., Papanikolaou, D., Farangitakis, G.P., Ruhnau, M., Lampridou, D., 2018. Expanding extension, subsidence and lateral segmentation within the Santorini - Amorgos basins during Quaternary: Implications for the 1956 Amorgos events, central - South Aegean Sea, Greece. Tectonophysics 722, 138–153. https://doi.org/10.1016/J.TECTO.2017.10.016.

Nyst, M., Thatcher, W., 2004. New constraints on the active tectonic deformation of the Aegean. J. Geophys. Res. 109, B11406. https://doi.org/10.1029/2003JB002830.

Okal, E., Synolakis, C., Uslu, B., Kalligeris, N., Voukouvalas, E., 2009. The 1956 earthquake and tsunami in Amorgos, Greece. Geophys. J. Int. 178, 1533–1554. https://doi.org/10.1111/j.1365-246X.2009.04237.x.

Papazachos, B.C., Karakostas, V.G., Papazachos, C.B., Scordilis, E.M., 2000. The geometry of the Wadati–Benioff zone and lithospheric kinematics in the Hellenic arc. Tectonophysics 319 (4), 275–300. https://doi.org/10.1016/S0040-1951(99)00299-1.

Perissoratis, C., Papadopoulos, G., 1999. Sediment instability and slumping in the southern Aegean Sea and the case history of the 1956 tsunami. Mar. Geol. 161, 287–305. https://doi.org/10.1016/S0025-3227(99)00039-0.

Ranjan, P., Konstantinou, K.I., 2020. Mapping intrinsic and scattering attenuation in the southern Aegean crust using S wave envelope inversion and sensitivity kernels derived from perturbation theory. J. Geophys. Res. Solid Earth 125, e2020JB020821. https://doi.org/10.1029/2020JB020821.

Ranjan, P., Konstantinou, K.I., Andinisari, R., 2019. Spatial distribution of random velocity inhomogeneities in the southern Aegean from inversion of S wave peak delay times. J. Geophys. Res. Solid Earth 124, 10393–10412. https://doi.org/10.1029/2018JB017198.

Reilinger, R., McClusky, S., Paradisis, D., Ergintav, S., Vernant, P., 2010. Geodetic constraints on the tectonic evolution of the Aegean region and strain accumulation along the Hellenic subduction zone. Tectonophysics 488, 22–30. https://doi.org/10.1016/j.tecto.2009.05.027.

Rontogianni, S., 2010. Comparison of geodetic and seismic strain rates in Greece by using a uniform processing approach to campaign GPS measurements over the interval 1994–2000. J. Geodyn. 50, 381–399. https://doi.org/10.1016/j.jog.2010.04.008.

Sakellariou, D., Sigurdsson, H., Alexandri, M., Carey, S., Rousakis, G., Nomikou, P., Georgiou, P., Ballas, D., 2010. Active tectonics in the Hellenic volcanic arc: the Kolumbo submarine volcanic zone. Bull. Geol. Soc. Greece 43 (2), 1056–1063. https://doi.org/10.12681/bgsg.11270.

Tape, W., Tape, C., 2013. The classical model for moment tensors. Geophys. J. Int. 195 (3), 1701–1720. https://doi.org/10.1093/gji/ggt302.

Vavryčuk, V., 2011. Tensile earthquakes: Theory, modeling, and inversion. J. Geophys. Res. 116, B12320. https://doi.org/10.1029/2011JB008770.

Vavryčuk, V., 2015. Moment tensor decompositions revisited. J. Seismol. 19, 231–252. https://doi.org/10.1007/s10950-014-9463-y.

Vavryčuk, V., Bohnhoff, M., Jechumtálová, Z., Kolář, P., Šílený, J., 2008. Non-double-couple mechanisms of microearthquakes induced during the 2000 injection experiment at the KTB site, Germany: a result of tensile faulting or anisotropy of a rock? Tectonophysics 456 (1–2), 74–93. https://doi.org/10.1016/j.tecto.2007.08.019.